21st Australasian Fluid Mechanics Conference
Adelaide, Australia
10-13 December 2018

Large Eddy Simulation and Dynamic Mode Decomposition of Internal Flow Structure of Pressure Swirl Atomizer

F. Vashahi[1], Sh. Rezaei[1] and Jeekeun Lee[2]

[1]Fluid Engineering Lab. Department of Mechanical System Engineering, Graduate School of Chonbuk National University, Jeonju, South Korea.

[2]Division of Mechanical System Engineering, Chonbuk National University, Jeonju, South Korea.

Abstract

The present work reports on the flow characteristics of a pressure swirl atomizer using Large Eddy Simulation (LES) using STAR-CCM+ commercial software from SIEMENS. Upon a primary RANS simulation, grids have locally refined by a factor of Kolmogorov length scale. A time-steps of 2e-6s with 2nd order discretization scheme was used. The internal and external flow field of the spray is investigated and the swirl-related features of the nozzle are described using the extracted data on two different grids. The helical vortex inside the nozzle revealed the interaction of the generated air-core with the liquid film attached to the discharge orifice wall. Fast Fourier Transforms (FFT) confirmed the quality of LES and presents the time-scales existing in the vicinity of the data extraction probes. the By analyzing the velocity wave structure formed from outside the nozzle due to swirling flow, the primary and secondary break-up regions are distinguished and the time lag between the two are computed. Using MATLAB, Dynamic Mode Decomposition (DMD) was applied to extract the dominant structures inside the nozzle. The first DMD mode demonstrated a helical Precessing Vortex Core (PVC) due to Vortex Breakdown (VB) and its effects on the air core.

Introduction

Nozzles are widely used in industrial applications. In particular, the pressure swirl atomizers owing to their wide range of applications -from simplex fuel nozzle in gas turbine combustors to the agricultural area- have been at the center of attention for many decades [4, 5]. Experimental and numerical investigations by previous sciences aided the understanding of the nozzles performance in terms of droplet size distribution. The prediction of air cone diameter was achieved by comparing pressure drops in nozzles with different diameters [2]. It was reported that the spray cone angle and discharge coefficient remains unaffected by the increase of flow inlet velocity, but may be disrupted by the variation of swirl number [3]. In addition, the use of k-ε turbulence models was justified comparing against experimental data.

It is anticipated that swirling flow development plays a vital role on the spray pattern. To this extent, with the aid of CFD and LES, the internal two-phase flow of a pressure swirl nozzle is explored. The Volume of Fluid (VOF) model is used to model the interface between the liquid and air in CFD software Star CCM+. Efforts were done to investigate the swirling flow at constant injection pressure inside the nozzle and correlations between the waves generated at the external flow field with their respective frequency is given.

Domain and Boundary Condition

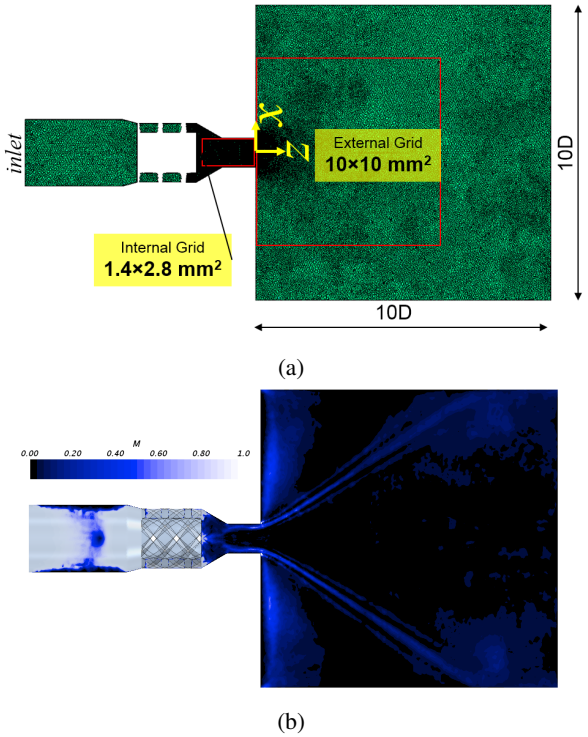

Figure 1: a) Grid density at the planar section and b) distribution of M-criterion on the cross-sectional plane.

Three-dimensional model was modeled by the STAR-CCM+ commercial package from Siemens. The two-phase incompressible flow Large Eddy Simulation (LES) was simulated via segregated velocity/pressure flow solver based on the SIMPLE algorithm with 2nd order convection scheme using Volume of Fluid (VOF) model. The Wall-adapting local eddy-viscosity (WALE) model was introduced by [6] was used to model the eddy viscosity with respect to its previously assessed agreement with the experimental data [7, 13–15, 18, 19]. Interfaces between the phases is obtained using the High-Resolution Interface Capturing (HRIC) scheme [16, 17].

The polyhedral unstructured mesh was developed with heavy local refinement at the throat of the nozzle to 15% of the base size. Constructing 8 prism layer stretched by a factor of 1.1 and a total thickness of 15μm, wall $y^+ \leq 1.0$ was computed within the entire region. Such configuration resulted in the total cell count of 3,303,926 cells and is presented in Fig. 1a.

M-criterion (M) is defined as the ratio of the mean of subgrid kinetic energy (k_{sgs}) to the mean total kinetic energy in the fol-

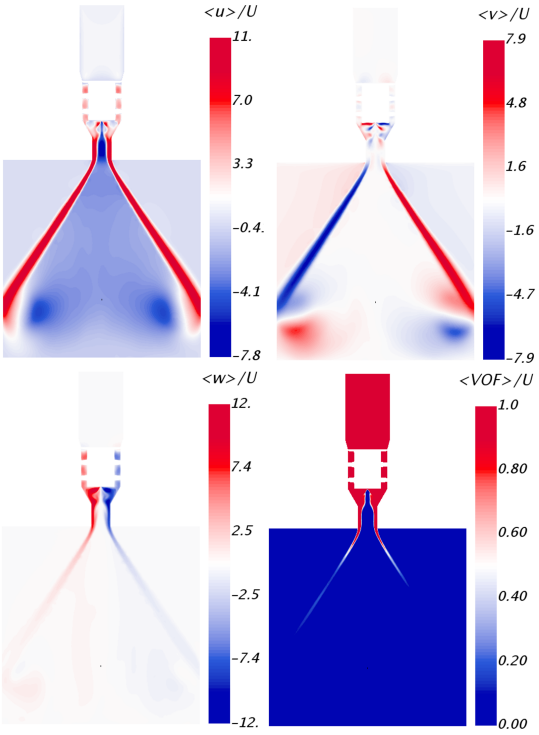

Figure 2: Time average fields from LES simulation. From left to right, normalized axial, radial and tangential velocity, and volume fraction, respectively. Volume fraction of 1.0 indicates 100% liquid and 0.0 depicts the 100% air region.

lowing manner

$$M = \frac{k_{sgs}}{k_{sgs} + k_{res.}} \leq 0.2 \quad (1)$$

and for LES, M should lies between 0 and 0.2 [8]. From Figure 1b, the region close to the inlet belongs to the modeled region with a higher ratio of subgrid kinetic energy. However, it is clear that the majority of cells fell below the 20% line, in particular, within the regions of interest as the nozzle throat and exit. The implicit unsteady scheme was applied with a 2ndorder temporal discretization and time-step (Δt) of $2 \times 10^{-6} s$ equal to $2\mu s$ was set. The Δt, was set as a conservative approach to save computation time. Within this circumstances the maximum Courant number reach to ≈3.5 within limited number of regions -in particular near the nozzle exit- but remained less than unity at other regions.

Fuel at the inlet and ambient air were defined as the two main Eulerian phases. The initial state of the simulation was considered as air and fuel is injected at the inlet with a constant mass flow rate of 0.0121 kg/s corresponding to inlet velocity of $U \approx 1.38 m/s$ and Reynolds number of ≈350. The Reynolds number is calculated based on the nozzle exit diameter of 1.5 mm, fuel density and dynamic viscosity of 960 kg/m^3 and 0.0058 Pa.s, respectively. The ambient was considered as pressure outlet condition as air with 0.0 gauge pressure. Walls are treated as no-slip.

Time-averaged Flow Field

Figure 2 represents the time-averaged fields on a cut section at the center of the nozzle. Combination of the intense recirculation region inside the nozzle and the distribution of volume fraction indicates the existence of the air core. The interaction of the recirculation region and the flow toward the nozzle exit produces a mushroom shape region upstream of the nozzle exit at the top of the swirl chamber. Although the axial velocity contour shows a giant recirculation zone at the ambient, yet the volume fraction contours show that the region mainly consists of air and no liquid is affected. The development region of each velocity component is also different. Flow emerges with mainly tangential component due to the swirl vanes inside the chamber. Then the axial velocity develops within the throat region and finally, the radial velocity starts to develop as the flow exit from the nozzle tip. The magnitudes of axial and tangential velocity are comparable while the radial velocity is relatively lower.

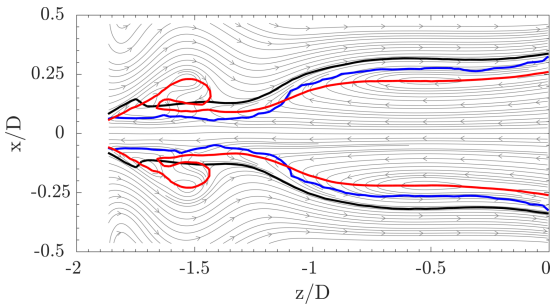

Figure 3: Internal flow structure presented on the internal grid introduced in Fig. 1a superimposed by the u and v velocity streamlines. Iso-lines of black, blue and red represent the 0.5 volume fraction, 0.0 pressure and 0.0 axial velocity, respectively.

Figure 3 demonstrates the flow field inside the nozzle. 5,000 samples on the internal grid depicted in Fig. 1a were extracted and averaged with sampling intervals of Δt=2e-6s. The streamlines of the axial and radial velocity components and iso-line of the zero axial velocity indicate the existence of two separate recirculation regions at the swirl chamber and throat of the nozzle. The mushroom structure of the volume fraction also can be clearly seen. The boundaries of the zero pressure lie between the 0.5 volume fraction zero axial velocity. The iso-lines indicate that owing to the positive pressure gradient due to the domination of the swirl component, flow is reversed on both the air and liquid phases where the liquid phase is less affected by the recirculation region. Within this circumstances and due to the interaction of air and liquid on the created interface, a highly complex unsteady flow is expected.

External Flow Analysis Method

In order to analyze the external flow field, the basic assumption is that due to the swirling motion at the exit of the nozzle, similarities between the signals acquired at the positive and negative side of the spray along the x/D direction exists. For the analysis presented in this section, it is important to first investigate the credibility of the assumption. Let's consider two points -here termed as Wave Point 1 and 2- along with the spray within the external region. The points share the same axial distance (z/D) from the swirler exit and positioned symmetrically with respect to the nozzle axis. The time series of axial velocity for these two points can be represented as Fig. 4. Performing cross-correlation, the time lag between the two can be computed and the signals with respect to their time

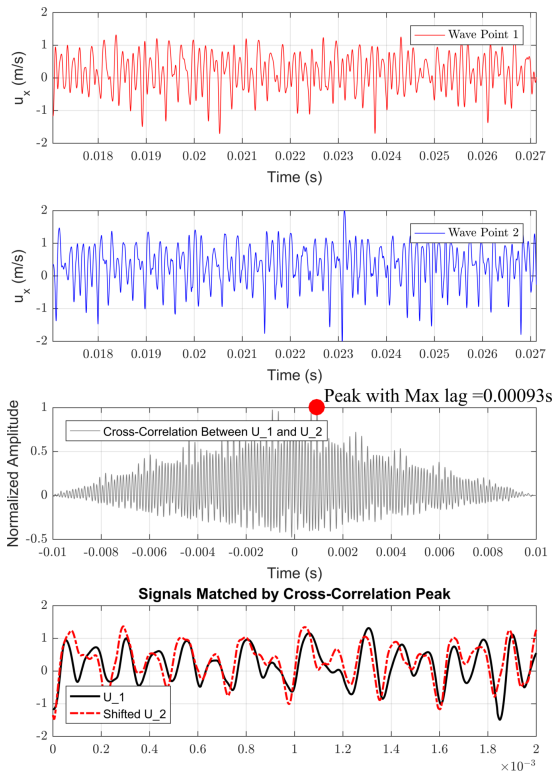

Figure 4: Top) Time series of axial velocity on two points, middle) Cross correlation of the two collected signals and bottom) the matched signal from the time-lag.

lag could be matched. The matched signals prove the basic assumption made since the signals matched almost perfect.

With establishing the similarities between the signals acquired at both side of the spray, we now investigate whether it remains intact further downstream of the spray. We turn to the Fast Fourier Transform (FFT) and compute the most dominant frequency of each signal. Fig. 5 shows a representative case of FFT computation at the given coordinate. One can note the Kolmogorov slope of (-5/3) indicating the quality of the LES grids. At this point, the most dominant frequency (f) is 8097Hz corresponding to equal Strouhal number (St) of 8.79 for both signals. Strouhal number is calculated by the orifice diameter of D=1.5 mm and inlet velocity of U=1.38m/s. Having the dominant frequency in hand and the inlet velocity, the corresponding wavelength can be given as $\lambda = u_{inlet}/f$. We

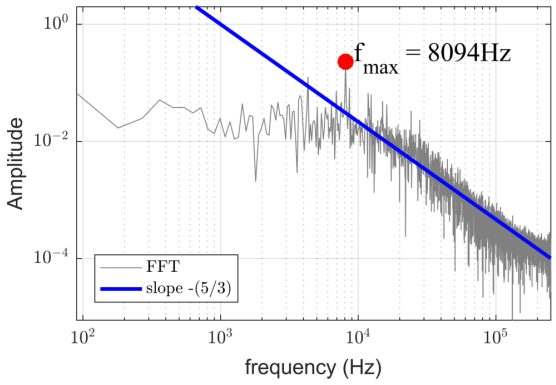

Figure 5: FFT sample at (x/D=0.6667, z/D=0.4).

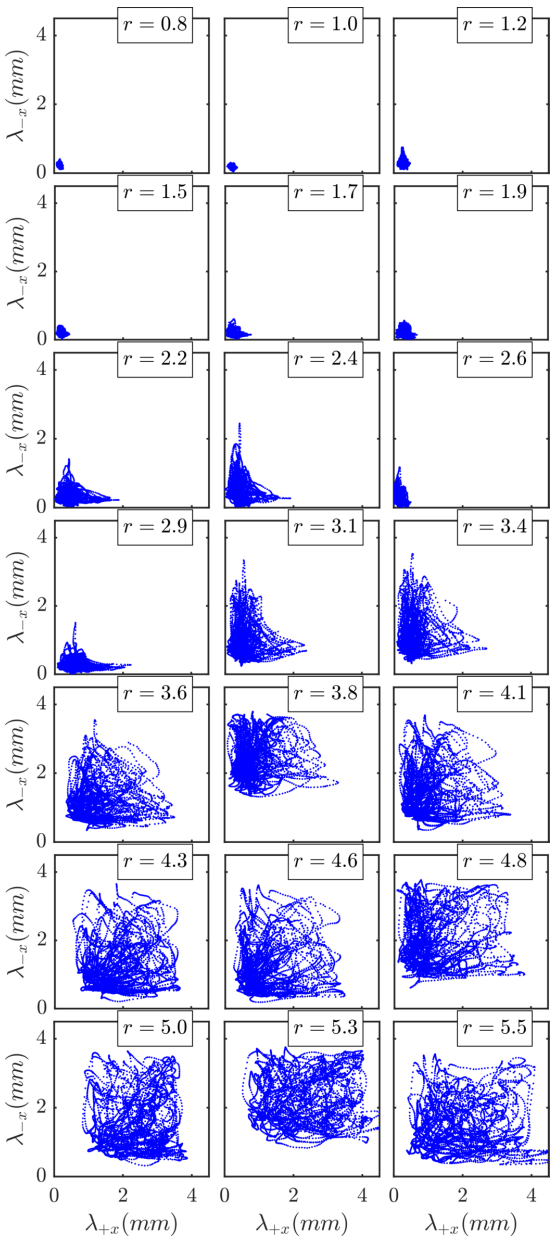

Figure 6: Wavelength distribution alongside the edge of the spray. $r = \sqrt{x/D^2 + z/D^2}$.

seek to perform the analysis on 21 points along the spray edge, from z/D=0 to z/D=4.0 downstream of the nozzle tip.

Spray Break-up Identification

Fig. 6 shows the scatter plot of wavelengths on the positive and negative side of the spray. The length of waves increases monotonically as the distance from the nozzle tip increases. However, between the r=2.4 and 2.6, the wavelength structure after excessive over-lengthening is disintegrated into smaller waves. From this point, the wavelength on both side again starts to increase and its spatial distribution relocated to the negative side of the spray. This indicates that for instance at r=3.8, longer waves are expected on the negative side and shorter ones on the positive side. However, further downstream at r=4.3, an intermittent behavior is observed where the position of longer and shorter waves are shifted to the opposite side of the spray.

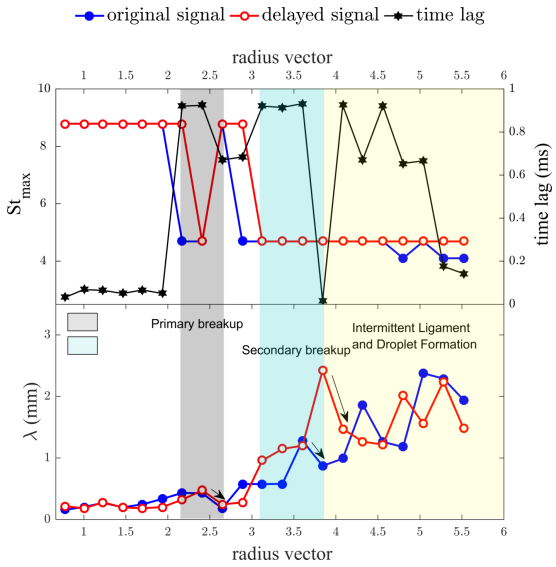

Figure 7: Distribution of the frequency peaks and wavelength for points along the spray edge.

Further downstream very stochastic behavior of the wavelength can be observed.

The reason behind such behavior could be investigated through the acquired peaks of FFT. Fig. 7 compares the wavelength and frequency of the waves. It can be seen that with an increase in radius vector (r), the averaged wavelength on the original signal (beginning of the swirl direction) starts to increase (r=2). At this point, the dominant frequency drops to half approximately and causing the time lag between the two signals to increase. This corresponds to a reduction in the wavelength and can be attributed to the primary break-up region at r=2.2. Along with the break-up, the time-lag between the two signal is reduced and the dominant frequency gains its original value. This is an indication of the primary break-up where although the spray is distorted, yet the ligaments still continue with the swirling motion and travel with the original frequency of the flow.

Moving along with the swirl direction on the edge of the spray, wavelength on the delayed signal starts to increase rapidly while the original signal remains constant. The increase in the wavelength on the delayed signal results in an increase in time-lag and causes a rapid decay in the frequency down to St=4.2 at r=3.0. With further increase in the delayed signal wavelength at r=3.6, with a sudden increase in delayed signal wavelength, the time lag and strouhal number decay significantly. This region is attributed to the secondary break-up with the spray. From this point forward, lower frequency movements of the drops and intermittent ligament and droplet formation is observed through variation in wavelength and time lag between the signals.

DMD Decomposition of the Internal Flow

The unsteady flow structure is demonstrated through Dynamic Mode Decomposition (DMD) analysis. The DMD approach, decomposes the data set into modes with distinct frequencies. However, it is usually not easy to distinguish the relevant frequencies with actual physical interpretation. Each DMD mode has a single characteristic frequency of oscillation and a growth/decay rate. Here we use the original DMD introduced by [9]. A great overview of the technique has been provided

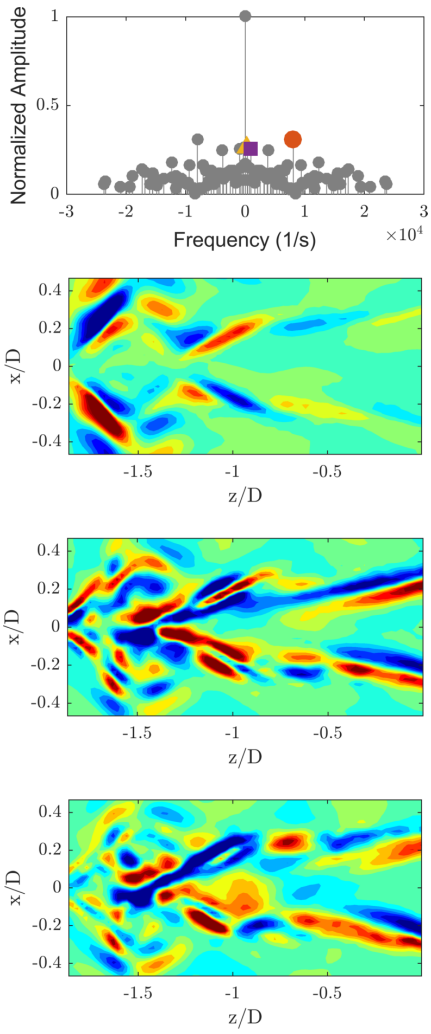

Figure 8: First 3 DMD modes.

in [11]. For further insight into DMD and its applications, the reader is referred to [1, 10, 12].

Fig. 8 represents the first three DMD modes from vorticity component. The in-plane vorticity is calculated as the curl of u and v velocity components. 2000 snapshots are employed and the performed DMD is rank 100. As indicated in the frequency vs. amplitude plot, the Most dominant DMD mode with the highest amplitude is the mean flow at(f=0) which is not plotted here and instead the first three running modes after the mean flow is given. The First vorticity mode indicates the existence of strong shear at the upstream of the chamber due to the bluff body vortex breakdown and interaction with the air core. The mode structure downstream consists of out-of-phase flow traveling downstream similar to the helical swirling motion.

The second mode shows strong out of phase lateral movement of the shear layer due to the change in the size of the air core inside and highlights the low-velocity core generated at x/D=0 and z/D-1.4. This region contains a mixture of air and liquid due to the upstream vortex breakdown and flow reversal from the nozzle exit as was demonstrated in the contour of volume fraction in Fig. 2. The third mode also shows the stochastic behavior due to the upstream vortex breakdown with traces of the second mode. However, it is not feasible to physically interpret the spatial field.

Conclusions

The internal and external flow structure of a pressure swirl atomizer was investigated through time-average data. The simulation data was acquired through Large Eddy Simulation performed via commercial code STAR-CCM+ from SIEMENS. It was found that the zero-pressure region inside the nozzle is sandwiched between the interface of air and liquid and zero-axial velocity. Where the zero axial velocity iso-line lies within the air core. Through FFT and cross-correlation of the signals at equally positioned points from the nozzle tip and estimation of wavelengths formed at the spray periphery, it was suggested that while the original signal is responsible for the primary break-up, the secondary break-up occurs at the opposite side of the spray. The unsteady flow structure inside the nozzle was then depicted with the of first three DMD modes. The modes depicted the existence of helical structures due to the swirling motion and strong lateral movement of the air/liquid interface at the throat region.

Acknowledgments

This work was carried out with the support of "Cooperative Research Program for Agriculture Science & Technology Development (Project No. PJ013819022018)" Rural Development Administration, Republic of Korea and was also partially funded by Korea Electric Power Corporation through Korea Electrical Engineering and Science Research Institute. Grant Number: 18B-022.

References

[1] Chen, K. K., Tu, J. H. and Rowley, C. W., Variants of dynamic mode decomposition: boundary condition, koopman, and fourier analyses, *Journal of nonlinear science*, **22**, 2012, 887–915.

[2] Datta, A. and Som, S., Numerical prediction of air core diameter, coefficient of discharge and spray cone angle of a swirl spray pressure nozzle, *International journal of heat and fluid flow*, **21**, 2000, 412–419.

[3] Halder, M., Dash, S. and Som, S., A numerical and experimental investigation on the coefficients of discharge and the spray cone angle of a solid cone swirl nozzle, *Experimental Thermal and Fluid Science*, **28**, 2004, 297–305.

[4] Lefebvre, A. H., *Gas turbine combustion*, CRC press, 1998.

[5] Lefebvre, A. H. and Ballal, D. R., *Gas turbine combustion: alternative fuels and emissions*, CRC press, 2010.

[6] Nicoud, F. and Ducros, F., Subgrid-scale stress modelling based on the square of the velocity gradient tensor, *Flow, turbulence and Combustion*, **62**, 1999, 183–200.

[7] Nicoud, F., Toda, H. B., Cabrit, O., Bose, S. and Lee, J., Using singular values to build a subgrid-scale model for large eddy simulations, *Physics of Fluids*, **23**, 2011, 085106.

[8] Pope, S., *Turbulent Flows*, Cambridge University Press, 2000.

[9] Schmid, P. J., Dynamic mode decomposition of numerical and experimental data, *Journal of fluid mechanics*, **656**, 2010, 5–28.

[10] Schmid, P. J., Li, L., Juniper, M. P. and Pust, O., Applications of the dynamic mode decomposition, *Theoretical and Computational Fluid Dynamics*, **25**, 2011, 249–259.

[11] Taira, K., Brunton, S. L., Dawson, S. T. M., Rowley, C. W., Colonius, T., McKeon, B. J., Schmidt, O. T., Gordeyev, S., Theofilis, V. and Ukeiley, L. S., Modal analysis of fluid flows: An overview, *AIAA Journal*, **55**, 2017, 4013–4041.

[12] Tu, J. H., Rowley, C. W., Luchtenburg, D. M., Brunton, S. L. and Kutz, J. N., On dynamic mode decomposition: theory and applications, *arXiv preprint arXiv:1312.0041*.

[13] Vashahi, F., Baek, B. J. and Lee, J., An experimental and les comparison of water-and air-based swirling flow test rigs in vertical and horizontal configurations, *Journal of Mechanical Science and Technology*, **31**, 2017, 3285–3295.

[14] Vashahi, F. and Lee, J., On the emerging flow from a dual-axial counter-rotating swirler; les simulation and spectral transition, *Applied Thermal Engineering*, **129**, 2018, 646 – 656.

[15] Vashahi, F., Lee, S. and Lee, J., Experimental and computational analysis of the swirling flow generated by an axial counter-rotating swirler in a rectangular model chamber using water test rig, *Journal of Engineering for Gas Turbines and Power*, **139**, 2017, 081501.

[16] Waclawczyk, T. and Koronowicz, T., Modeling of the wave breaking with cicsam and hric high resolution schemes, in *Proceedings of the European Conference on Computational Fluid Dynamics*, 2006.

[17] Wacławczyk, T. and Koronowicz, T., Comparison of cicsam and hric high-resolution schemes for interface capturing, *Journal of theoretical and applied mechanics*, **46**, 2008, 325–345.

[18] Wang, P., Bai, X.-S., Wessman, M. and Klingmann, J., Large eddy simulation and experimental studies of a confined turbulent swirling flow, *Physics of Fluids*, **16**, 2004, 3306–3324.

[19] Weickert, M., Teike, G., Schmidt, O. and Sommerfeld, M., Investigation of the les wale turbulence model within the lattice boltzmann framework, *Computers & Mathematics with Applications*, **59**, 2010, 2200–2214.